

INFRARED [Fe II] EMISSION LINES FROM RADIATIVE ATOMIC SHOCKS

BON-CHUL KOO^{1,2}, JOHN, C. RAYMOND³, AND HYUNG-JEONG KIM¹

¹Department of Physics and Astronomy, Seoul National University, Gwanak-gu, Seoul 151-747, Korea;
koo@astro.snu.ac.kr, hjkim@astro.snu.ac.kr

²Visiting Professor, Korea Institute of Advanced Study, Seoul 02455, Korea

³Harvard-Smithsonian Center for Astrophysics, 60 Garden Street, Cambridge, MA 02138, USA;
jraymond@cfa.harvard.edu

Received April 1, 2016; accepted April 2, 2016

Abstract: [Fe II] emission lines are prominent in the infrared (IR), and they are important diagnostic tools for radiative atomic shocks. We investigate the emission characteristics of [Fe II] lines using a shock code developed by Raymond (1979) with updated atomic parameters. We first review general characteristics of IR [Fe II] emission lines from shocked gas, and derive [Fe II] line fluxes as a function of shock speed and ambient density. We have compiled the available IR [Fe II] line observations of interstellar shocks and compare them to the ratios predicted from our model. The sample includes both young and old supernova remnants in the Galaxy and the Large Magellanic Cloud and several Herbig-Haro objects. We find that the observed ratios of IR [Fe II] lines generally fall on our grid of shock models, but the ratios of some mid-infrared lines, e.g., [Fe II] 35.35 μm /[Fe II] 25.99 μm , [Fe II] 5.340 μm /[Fe II] 25.99 μm , and [Fe II] 5.340 μm /[Fe II] 17.94 μm , are significantly offset from our model grid. We discuss possible explanations and conclude that the uncertainty in atomic rates might be the major source of uncertainty, while uncertainties in the shock modeling and the observations certainly exist.

Key words: atomic processes: hydrodynamics: infrared: ISM: shock waves

1. INTRODUCTION

Shocks are ubiquitous in the interstellar medium (ISM). Supernova (SN) blast waves, stellar winds, and outflows/jets from young stellar objects are among diverse driving sources. The shocks associated with these sources generally manifest themselves in various metallic ionic lines, which may be compared to theoretical models of shock emission lines to reveal the physical conditions of their environments and also to infer the nature of driving sources. Most of these sources, however, are located in the Galactic plane where the extinction can be so large that optical emission lines are not observable.

In radiative atomic shocks, in the NIR/MIR band, the forbidden lines from Fe⁺ are usually most prominent. There are some unique features that make [Fe II] lines strong (McKee, Chernoff, & Hollenbach 1984; Hollenbach, Chernoff, & McKee 1989; Oliva, Moorwood, & Danziger 1989). First, the Fe⁺ ion has many (16) levels with low excitation energies, so that these levels are easily excited in shocked gas and the transitions among them result in many lines in IR, particularly in the NIR band. Second, the ionization potential of an Fe atom is 7.9 eV (< 13.6 eV), so that there is an extended region behind the shock front where Fe is ionized to Fe⁺ by FUV radiation from the shock front while H atoms are mostly neutral. This is in contrast to photoionized regions where Fe atoms are mostly in higher ionization stages unless the ionizing radiation

is hard enough to penetrate deep into interstellar cloud, such as in active galactic nuclei. Third, the Fe abundance can be enhanced due to grain destruction by shocks and can approach its cosmic abundance, i.e., Fe/H = 3.47×10^{-5} by number (Asplund et al. 2009), while in the general ISM, 99% of Fe is locked in dust. In supernova remnants (SNRs), the newly-synthesized Fe from SN can enhance the Fe abundance too. Therefore, [Fe II] emission lines from shocked gas are stronger than those from photoionized regions, e.g. [Fe II]/Pa β =1–10 compared to 0.01 (Mouri et al. 2000; Koo & Lee 2015). That makes these lines very useful for the study of interstellar shocks (e.g., Dinerstein 1995; Nisini 2008).

Theoretical calculations of IR [Fe II] lines from interstellar shocks have been done by several groups, i.e., McKee, Chernoff, & Hollenbach (1984); Hollenbach, Chernoff, & McKee (1989); Hartigan et al. (2004). McKee, Chernoff, & Hollenbach (1984) calculated [Fe II] 1.257 μm intensities for 40 and 100 km s⁻¹ shocks propagating into atomic gas of ambient hydrogen nuclei density $n_0 = 10 \text{ cm}^{-3}$ and also a 100 km s⁻¹ shock into atomic gas of $n_0 = 100 \text{ cm}^{-3}$. Hollenbach, Chernoff, & McKee (1989) calculated the [Fe II] 1.257 and 1.644 μm intensities for dissociative *J*-shocks with speeds of 30–150 km s⁻¹ incident upon molecular gas of $n_0 = 10^3$ – 10^4 cm^{-3} . The above works included grain destruction. Hartigan et al. (2004) calculated the intensities of strong NIR [Fe II] lines for relatively slow shocks (30–50 km s⁻¹) propagating through atomic gas of $n_0 = 10^3$ – 10^5 cm^{-3} appropriate for outflows from protostellar objects. Recently,

CORRESPONDING AUTHOR: B.-C. Koo

Allen et al. (2008) presented a detailed grid of shock models for $v_s = 100\text{--}1,000\text{ km s}^{-1}$ and $n_0 = 0.01\text{--}1,000\text{ cm}^{-3}$ using the shock modeling code MAPPINGS III (Dopita & Sutherland 1995, 1996), but they do not tabulate the Fe line intensities.

In this paper, we use the shock code of Raymond (1979) and Cox & Raymond (1985) with updated atomic parameters to model [Fe II] emission lines from atomic shocks. One of the motivations of this work is the availability of revised atomic constants for the [Fe II] lines. Fe^+ is a complex ion and its atomic constants, e.g., coefficients of collision rates and radiative transitions, are still not accurate. Another motivation is the accumulation of IR [Fe II] line observations of interstellar shocks, including 1 to $2.5\ \mu\text{m}$ ground-based spectra and *Spitzer* spectra at longer wavelengths. It is worthwhile to compare the observed [Fe II] emission line parameters of these sources and to confirm their similarities and differences. The organization of this paper is as follows. In § 2, we summarize the atomic constants and also the parameters of strong [Fe II] lines. We briefly discuss the basic applications of [Fe II] lines, as well. In § 3, we investigate the shock structure and the physical properties of the [Fe II]-line emitting layers. Physical variables, e.g., temperature and density, usually vary through the emitting layer, and we discuss the significance of the parameters derived by solving rate equations. We also derive [Fe II] line fluxes as a function of shock speed ($20\text{--}200\text{ km s}^{-1}$) and density ($10\text{--}10^3\text{ cm}^{-3}$), and compare them to those of previous studies. In § 4, we present shock grids for NIR and MIR [Fe II] emission lines and compare them to the available observations of interstellar shocks. In § 5, we conclude our paper.

2. ATOMIC CONSTANTS AND BASIC APPLICATIONS OF [Fe II] LINES

2.1. Atomic Constants

The Fe^+ ion has four ground terms, a^6D ($3d^64s$), a^4F ($3d^7$), a^4D ($3d^64s$), and a^4P ($3d^7$), each of which has 3–5 closely-spaced levels to form a 16 level system (Pradhan & Nahar 2011; see Fig. 1). The energy gap between the ground level and the excited levels is less than $2 \times 10^4\text{ K}$, so that these levels are easily excited in postshock cooling region, and the emission lines resulting from the transitions among them appear in near-to far-IR bands. The energy gap to the next coupled higher-energy term (b^4P) is 0.9 eV, so that it is usually acceptable to consider only these 16 levels in computing the line intensities from shocked gas. (There are several other terms between a^4P and b^4P , but they are weakly coupled. See Pradhan & Nahar (2011).) There are numerous [Fe II] lines at visual wavelengths, but they are not included in our models.

The atomic parameters necessary for the calculation of [Fe II] forbidden lines have been continuously updated with the advance of computing power and theoretical modeling. The Maxwellian-averaged collision strengths for electron-impact excitation have

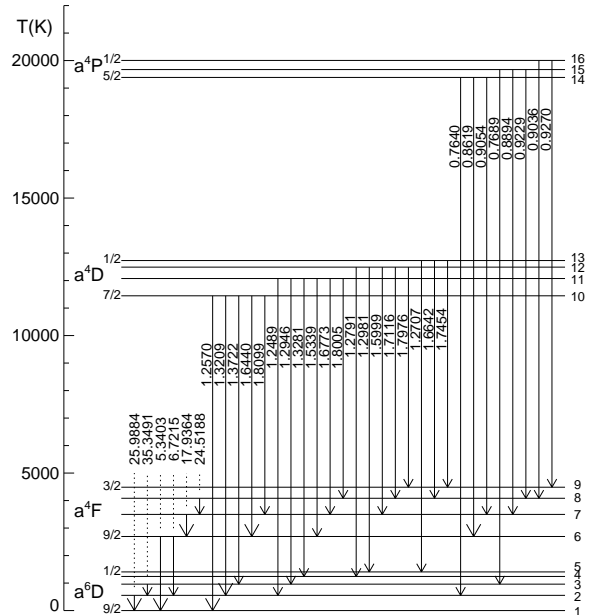


Figure 1. Energy level diagram for the first four low-lying terms of Fe^+ . For convenience, we numbered the levels consecutively by 1 to 16 from the ground level. The transitions resulting strong lines in Table 1 are marked with their wavelengths (in μm). Relatively strong lines (i.e., the lines with intensities stronger than 30% of the $1.644\ \mu\text{m}$ line in Table 1) are marked by thick solid lines. The temperature scale bar on the left shows the excitation energies of the levels.

been recently calculated by Ramsbottom et al. (2007) who included the 100 LS terms belonging to the basis configurations $3d^64s$, $3d^7$, and $3d^64p$. They showed that their results differ considerably from previous theoretical works (e.g., Zhang & Pradhan 1995). We find that the ratio of the collision strengths of Ramsbottom et al. (2007) to those of Zhang & Pradhan (1995) ranges from 0.35 to 2.3 with a mean of 0.99 ± 0.29 at 5,000 K. More recently, Bautista et al. (2015) conducted a major study of the [Fe II] atomic rates, making some new theoretical calculations, comparing the predictions with those of earlier work, and elucidating the reasons for discrepancies among them. Radiative transition probabilities (Einstein A coefficients) in the literature also show considerable scatter. For example, the theoretical A -values for the two strongest 1.257 and $1.644\ \mu\text{m}$ lines range $4.83\text{--}5.27 \times 10^{-3}\text{ s}^{-1}$ and $4.65\text{--}5.07 \times 10^{-3}\text{ s}^{-1}$, respectively (Nussbaumer & Storey 1988; Quinet, Le Dourneuf, & Zeippen 1996; Deb & Hibbert 2010, 2011; Bautista et al. 2015). This results in the considerable dispersion (1.18–1.36) in the expected [Fe II] $1.257/1.644\ \mu\text{m}$ intensity ratio, which is used to derive the extinction (Koo & Lee 2015). On the other hand, Rodríguez-Ardila et al. (2004); Smith & Hartigan (2006); Giannini et al. (2015) empirically derived the ratio between 0.98 and 1.49 from observations of nearby stellar objects. We will use

Table 1
Strong [Fe II] lines from transitions among the levels in ground terms

| Level ID | | Levels | | λ | T_{ex} | A_{21} | n_{cr} | Line intensity | | |
|----------|---|--------|--------|-------------------|-----------------|---------------------|----------------------|----------------|--------|------------------------|
| u | l | upper | lower | (μm) | (K) | (s^{-1}) | (cm^{-3}) | $n_e = 10^3$ | 10^4 | 10^5 cm^{-3} |
| 2 | 1 | a6D7/2 | a6D9/2 | 25.9884 | 554 | 2.14e-03 | 3.40e+03 | 0.51 | 0.34 | 0.17 |
| 3 | 2 | a6D5/2 | a6D7/2 | 35.3491 | 961 | 1.58e-03 | 2.28e+03 | 0.11 | 0.10 | 0.06 |
| 6 | 1 | a4F9/2 | a6D9/2 | 5.3403 | 2,694 | 1.30e-04 | 4.44e+02 | 0.99 | 0.30 | 0.07 |
| 6 | 2 | a4F9/2 | a6D7/2 | 6.7215 | 2,694 | 1.16e-05 | 4.44e+02 | 0.07 | 0.02 | 0.00 |
| 7 | 6 | a4F7/2 | a4F9/2 | 17.9364 | 3,496 | 5.86e-03 | 1.53e+04 | 0.24 | 0.44 | 0.41 |
| 8 | 7 | a4F5/2 | a4F7/2 | 24.5188 | 4,083 | 3.93e-03 | 1.05e+04 | 0.05 | 0.11 | 0.13 |
| 10 | 1 | a4D7/2 | a6D9/2 | 1.2570 | 11,446 | 5.27e-03 | 3.28e+04 | 1.36 | 1.36 | 1.36 |
| 10 | 2 | a4D7/2 | a6D7/2 | 1.3209 | 11,446 | 1.49e-03 | 3.28e+04 | 0.37 | 0.37 | 0.37 |
| 10 | 3 | a4D7/2 | a6D5/2 | 1.3722 | 11,446 | 9.72e-04 | 3.28e+04 | 0.23 | 0.23 | 0.23 |
| 10 | 6 | a4D7/2 | a4F9/2 | 1.6440 | 11,446 | 5.07e-03 | 3.28e+04 | 1.00 | 1.00 | 1.00 |
| 10 | 7 | a4D7/2 | a4F7/2 | 1.8099 | 11,446 | 1.12e-03 | 3.28e+04 | 0.20 | 0.20 | 0.20 |
| 11 | 2 | a4D5/2 | a6D7/2 | 1.2489 | 12,074 | 3.54e-04 | 2.80e+04 | 0.01 | 0.03 | 0.06 |
| 11 | 3 | a4D5/2 | a6D5/2 | 1.2946 | 12,074 | 2.20e-03 | 2.80e+04 | 0.05 | 0.17 | 0.33 |
| 11 | 4 | a4D5/2 | a6D3/2 | 1.3281 | 12,074 | 1.30e-03 | 2.80e+04 | 0.03 | 0.10 | 0.19 |
| 11 | 6 | a4D5/2 | a4F9/2 | 1.5339 | 12,074 | 2.64e-03 | 2.80e+04 | 0.05 | 0.18 | 0.33 |
| 11 | 7 | a4D5/2 | a4F7/2 | 1.6773 | 12,074 | 2.11e-03 | 2.80e+04 | 0.04 | 0.13 | 0.24 |
| 11 | 8 | a4D5/2 | a4F5/2 | 1.8005 | 12,074 | 1.55e-03 | 2.80e+04 | 0.03 | 0.09 | 0.17 |
| 12 | 4 | a4D3/2 | a6D3/2 | 1.2791 | 12,489 | 2.69e-03 | 2.50e+04 | 0.03 | 0.11 | 0.25 |
| 12 | 5 | a4D3/2 | a6D1/2 | 1.2981 | 12,489 | 1.17e-03 | 2.50e+04 | 0.01 | 0.05 | 0.11 |
| 12 | 7 | a4D3/2 | a4F7/2 | 1.5999 | 12,489 | 3.53e-03 | 2.50e+04 | 0.03 | 0.11 | 0.26 |
| 12 | 8 | a4D3/2 | a4F5/2 | 1.7116 | 12,489 | 9.93e-04 | 2.50e+04 | 0.01 | 0.03 | 0.07 |
| 12 | 9 | a4D3/2 | a4F3/2 | 1.7976 | 12,489 | 1.81e-03 | 2.50e+04 | 0.01 | 0.05 | 0.12 |
| 13 | 5 | a4D1/2 | a6D1/2 | 1.2707 | 12,729 | 3.60e-03 | 2.80e+04 | 0.02 | 0.07 | 0.16 |
| 13 | 8 | a4D1/2 | a4F5/2 | 1.6642 | 12,729 | 4.00e-03 | 2.80e+04 | 0.01 | 0.06 | 0.14 |
| 13 | 9 | a4D1/2 | a4F3/2 | 1.7454 | 12,729 | 2.11e-03 | 2.80e+04 | 0.01 | 0.03 | 0.07 |
| 14 | 2 | a4P5/2 | a6D7/2 | 0.7640 | 19,387 | 1.17e-02 | 2.13e+05 | 0.05 | 0.10 | 0.32 |
| 14 | 6 | a4P5/2 | a4F9/2 | 0.8619 | 19,387 | 2.73e-02 | 2.13e+05 | 0.11 | 0.22 | 0.66 |
| 14 | 7 | a4P5/2 | a4F7/2 | 0.9054 | 19,387 | 7.07e-03 | 2.13e+05 | 0.03 | 0.05 | 0.16 |
| 15 | 3 | a4P3/2 | a6D5/2 | 0.7689 | 19,673 | 1.22e-02 | 2.12e+05 | 0.03 | 0.05 | 0.21 |
| 15 | 7 | a4P3/2 | a4F7/2 | 0.8894 | 19,673 | 1.70e-02 | 2.12e+05 | 0.03 | 0.06 | 0.25 |
| 15 | 8 | a4P3/2 | a4F5/2 | 0.9229 | 19,673 | 9.87e-03 | 2.12e+05 | 0.02 | 0.03 | 0.14 |
| 16 | 4 | a4P1/2 | a6D3/2 | 0.7667 | 20,006 | 1.13e-02 | 2.28e+05 | 0.00 | 0.02 | 0.09 |
| 16 | 8 | a4P1/2 | a4F5/2 | 0.9036 | 20,006 | 1.24e-02 | 2.28e+05 | 0.00 | 0.02 | 0.08 |
| 16 | 9 | a4P1/2 | a4F3/2 | 0.9270 | 20,006 | 1.64e-02 | 2.28e+05 | 0.01 | 0.02 | 0.11 |

We list all [Fe II] lines resulting from transitions among the levels in four ground terms and brighter than 5% of [Fe II] 1.644 μm line in statistical equilibrium at densities 10^3 – 10^5 cm^{-3} and at $T_e = 7,000 \text{ K}$. In the table, T_{ex} = excitation temperature of the upper level, A_{21} = Einstein A coefficient, n_{cr} = critical density at $T_e = 7,000 \text{ K}$, and the last three columns = line intensities relative to [Fe II] 1.644 μm line at $n_e = 10^3, 10^4$ and 10^5 cm^{-3} assuming statistical equilibrium at $T_e = 7,000 \text{ K}$. The absolute intensity of [Fe II] 1.644 μm line for $N(\text{H}) = 10^{20} \text{ cm}^{-2}$ are 0.00234, 0.0136, and 0.0392 $\text{ergs cm}^{-2} \text{ s}^{-1}$ when $n_e = 10^3, 10^4$ and 10^5 cm^{-3} , respectively, assuming that Fe abundance is cosmic abundance, i.e., $X(\text{Fe}/\text{H}) = 3.47 \times 10^{-5}$ in number, and that all Fe is singly ionized. For the identification of upper and lower levels, see the energy diagram in Figure 1.

the effective collision strengths of Ramsbottom et al. (2007) and the A values of Deb & Hibbert (2011) for the shock code calculation. As we will show in § 2.2, the atomic constants of Bautista et al. (2015) yield line ratios that poorly match the observed ratios for some MIR lines, and furthermore they provided effective collision strengths only at temperatures above 5,000 K, while, in low-velocity shocks, a significant contribution to the MIR [Fe II] lines comes from regions at lower temperatures (see § 3).

Table 1 lists parameters of strong [Fe II] lines which are brighter than 5% of the 1.644 μm line in statistical equilibrium at densities 10^3 – 10^5 cm^{-3} and at $T_e = 7,000 \text{ K}$. (For completeness, we have included optical lines resulting from the transitions from a⁴P term.)

The critical density of level j is defined by

$$n_{\text{cr}} \equiv \Sigma A_{ji}(j > i) / \Sigma C_{ij}(j \neq i) \quad (1)$$

where ΣC_{ij} is the collisional (de-)excitation coefficient averaged over a Maxwellian-velocity distribution at temperature T_e (e.g., Draine 2011). The critical densities of NIR [Fe II] lines are 2.7 – $3.4 \times 10^4 \text{ cm}^{-3}$ at $T_e = 7,000 \text{ K}$ while they are lower (4.8×10^2 – $1.7 \times 10^4 \text{ cm}^{-3}$) for MIR/FIR [Fe II] lines and higher ($2.2 \times 10^5 \text{ cm}^{-3}$) for optical lines.

In order to use the [Fe II] lines to estimate the iron abundance, we need to know the fraction of Fe in Fe II. In radiative shock waves, the gas cools more rapidly from the postshock temperature than the recombination times of most ions, so that the gas is not in ionization equilibrium. In addition, photoionization of the

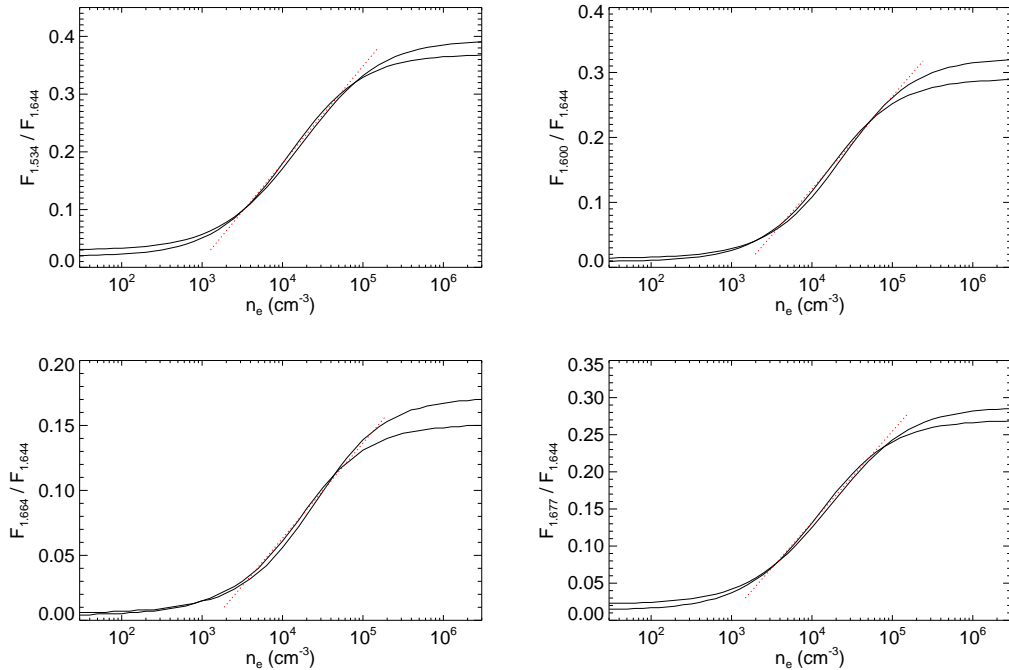


Figure 2. Density sensitive NIR [Fe II] line ratios as a function of electron density for gas in statistical equilibrium at temperatures 5,000 K and 10,000 K by thick and thin black lines, respectively. The dotted red lines are analytic approximations at 5,000 K (see text).

gas below about 10,000 K dominates the ionization state in shocks faster than about 100 km s^{-1} . The most important parameters are the Fe II collisional ionization rate, which Arnaud & Raymond (1992) determined from the laboratory measurements of Montague et al. (1984), the Fe II photoionization cross section, which we take from Reilman & Manson (1979) and the Fe III dielectronic and radiative recombination rates, for which we use Arnaud & Raymond (1992), and the Fe III+H charge transfer rate (Neufeld & Dalgarno 1987). The photoionization cross section we use is about 20% smaller than that of Verner et al. (1996), which is within the uncertainties. The dielectronic recombination rates differ significantly from those given by Nahar (1997), but the charge transfer rate dominates in the regions where it matters.

2.2. Basic Applications

2.2.1. NIR [Fe II] lines

One of the most useful applications of the NIR [Fe II] lines is to measure extinction. There are lines originating from the same upper levels, the ratios of which are functions of only the Einstein A coefficients (and their wavelengths). Their observed ratios provide an accurate measure of extinction to the emitting region. The two strong [Fe II] lines at 1.257 and 1.644 μm are such lines. If we adopt $A_{1.257}/A_{1.644} = 1.04$ (Deb & Hibbert 2011), the intrinsic ratio of their line intensities $j_{1.257}/j_{1.644} = 1.36$, so that the extinction (in mag) difference at 1.257 and 1.644 μm (ΔA_{JH}) can

be derived from

$$\Delta A_{JH} = 1.086 \log \left(\frac{F(1.257)/F(1.644)}{[F(1.257)/F(1.644)]_{\text{int}}} \right) \quad (2)$$

where $[F(1.257)/F(1.644)]_{\text{int}} (= 1.36)$ is the intrinsic line flux ratio. According to Bautista et al. (2015), the uncertainty in the intrinsic ratio is $\sim 20\%$, which yields an uncertainty of 0.09 mag in ΔA_{JH} . This corresponds to $A_V \approx 0.9$ mag for the Galactic extinction curve with $R_V = 3.1$. There are a couple of observable NIR lines sharing the same upper state, e.g., 1.321 μm and 1.372 μm lines (see Figure 1 and Table 1). There are also [Fe II] lines at 0.90–0.95 μm sharing their upper levels but they are weak (see Figure 1 and Table 1).

Another useful application is density diagnosis. There are several lines of comparable excitation energies, the ratios of which are mainly a function of electron density (n_e) of the emitting region, depending only weakly on temperature (T_e). Figure 2 shows four representative line ratios $r_{1.534/1.644} \equiv F(1.534)/F(1.644)$, $r_{1.600/1.644} \equiv F(1.600)/F(1.644)$, $r_{1.664/1.644} \equiv F(1.664)/F(1.644)$, and $r_{1.677/1.644} \equiv F(1.677)/F(1.644)$ for gas at temperature 5,000 K and 10,000 K. At low densities ($n_e \ll n_{\text{cr}}$), their ratios are equal to the ratio of collisional excitation rates, while at high densities ($n_e \gg n_{\text{cr}}$), their ratios are given by the ratio of spontaneous deexcitation rates. These line ratios can be used as a density diagnostic for $n_e = 10^3$ – 10^5 cm^{-3} . Convenient linear approximations that can be

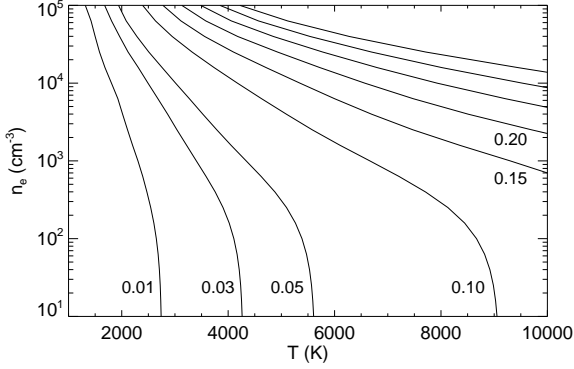


Figure 3. [Fe II] 0.8619 μm /[Fe II] 1.257 μm intensity ratios of thermal gas in statistical equilibrium in (T, n_e) plane. The contours of constant intensity ratios are plotted. Above 0.20, the contours are equally spaced in steps of 0.05.

used for $n_e = 3 \times 10^3$ to $8 \times 10^4 \text{ cm}^{-3}$ are

$$n_e = 10^{2.93+5.95r_{1.534/1.644}}, \quad 0.10 \leq r_{1.534/1.644} \leq 0.32 \quad (3)$$

$$n_e = 10^{3.16+7.01r_{1.600/1.644}}, \quad 0.06 \leq r_{1.600/1.644} \leq 0.24 \quad (4)$$

$$n_e = 10^{3.14+13.7r_{1.664/1.644}}, \quad 0.03 \leq r_{1.664/1.644} \leq 0.13 \quad (5)$$

$$n_e = 10^{2.93+8.14r_{1.677/1.644}}, \quad 0.07 \leq r_{1.677/1.644} \leq 0.23 \quad (6)$$

The maximum error of the above fits in electron density is less than 15%.

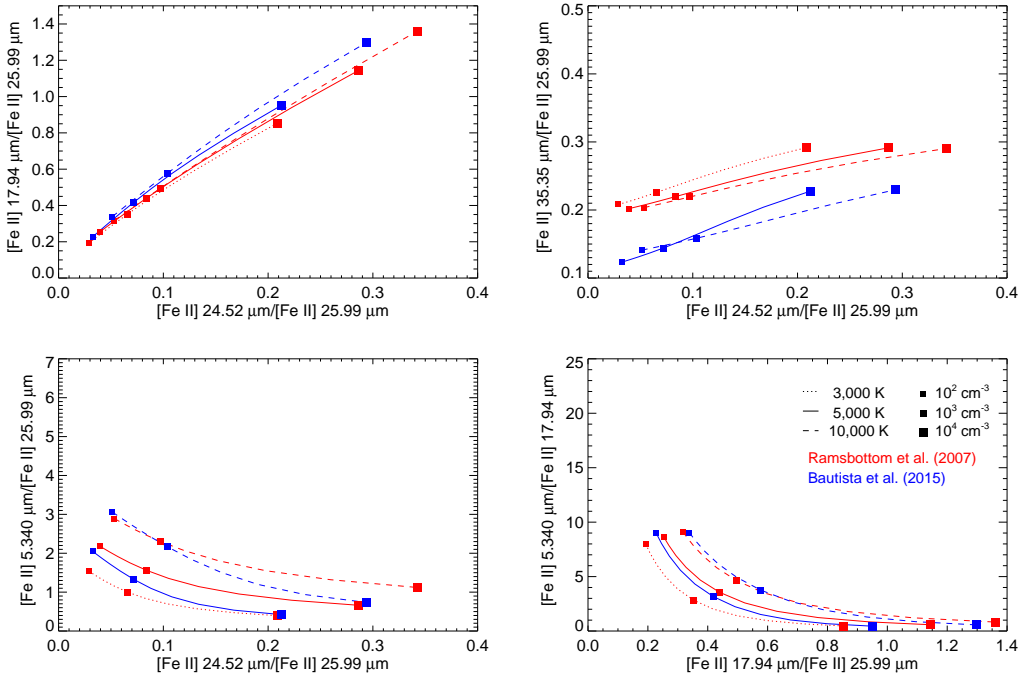


Figure 4. MIR [Fe II] line intensity ratios for thermal gas in statistical equilibrium at $T = 3,000, 5,000,$ and $10,000 \text{ K}$. Along each line, squares mark electron densities of $10^2, 10^3,$ and 10^4 cm^{-3} . The red lines represent the results obtained by using the effective collision strengths of Ramsbottom et al. (2007) and the A values of Deb & Hibbert (2011), while the blue lines are the results obtained by using those of Bautista et al. (2015).

If the electron density is known from the above, then the ratio of [Fe II] lines with considerably different excitation energies can be used for temperature diagnosis, although this requires observations of [Fe II] lines in different bands. Figure 3 is a diagnostic diagram using the ratio of 0.8619 μm and 1.257 μm lines, which are the two strongest lines from a^4P and a^4D terms to a^6D term, respectively. This may be compared to similar plots in previous studies, e.g., Figure 8 of Graham et al. (1990). In shocked gas, these lines originate from a region at $\sim 7,000 \text{ K}$ (see § 3.2), so the temperature diagnosis using [Fe II] lines is not particularly useful for interstellar shocks.

2.2.2. MIR [Fe II] lines

MIR [Fe II] lines are not useful for extinction measurement. There are 5.340 μm and 6.722 μm lines sharing the upper level ($a^4F_{9/2}$), but the 6.722 μm line is weak, i.e., their intrinsic intensity ratio $F(6.722)/F(5.340) = 0.071$ (Table 1). Also, the effect on MIR line intensities will be small unless the extinction is very large.

Intensity ratios of MIR [Fe II] lines may be used for density diagnosis, but they are rather temperature sensitive. In Figure 4, we plot the contours of constant temperatures at $n_e = 10^2$ to 10^4 cm^{-3} in the plane of the intensity ratios of strong MIR lines. The dependence of ratios on n_e and T can be understood by noting that the 25.99 μm and 35.35 μm lines have comparable T_{ex} (550–960 K) and n_{cr} (2.3 – $3.4 \times 10^3 \text{ cm}^{-3}$), while the 17.94 μm and 24.52 μm lines have comparable T_{ex}

(3,500–4,100 K) and n_{cr} ($1.1\text{--}1.5 \times 10^4 \text{ cm}^{-3}$) that are higher than those of the former lines (Table 1). Therefore, the intensity ratio of the latter to the former lines will increase with density as well as with temperature. On the other hand, the $5.340 \mu\text{m}$ line has a much lower critical density $n_{\text{cr}} (= 4.4 \times 10^2 \text{ cm}^{-3})$ and T_{ex} of 2,700 K, so that the intensity ratio of $5.340 \mu\text{m}$ to the other MIR lines will decrease with density. In addition to these, Figure 4 shows that the ratios $F(17.94)/F(25.99)$ and $F(24.52)/F(25.99)$ are proportional each other, nearly independent of temperature and density (upper left frame), implying $F(24.52)/F(17.94) \sim 0.4$.

In Figure 4, the red lines represent the results obtained by using the effective collision strengths of Ramsbottom et al. (2007) and the A values of Deb & Hibbert (2011), while the blue lines are the results obtained by using those of Bautista et al. (2015)¹. We note that the two sets of atomic constants yield $F(24.52)/F(25.99)$ ratios that are comparable at small n_e but considerably, e.g., by a factor of 1.4 at 5,000 K, different at $n_e = 10^4 \text{ cm}^{-3}$. They also yield $F(35.35)/F(25.99)$ ratios that differ by a factor of ~ 1.5 across most of the density range. These differences between the two results should be mostly due to the differences in collision strengths because the radiative transition rates for strong lines are almost the same except for a $^4\text{F}_{9/2}$ level where the $5.340 \mu\text{m}$ line originates. For the $5.340 \mu\text{m}$ line, the A -value of Bautista et al. (2015) is smaller than that of Deb & Hibbert (2011) by a factor of 2. The collision strengths of Bautista et al. (2015) are generally smaller than those of Ramsbottom et al. (2007) by a factor of $\lesssim 3$ (see their Table 8). As we will see in § 4, the result of Ramsbottom et al. (2007) is in better agreement with the observations, but it also poorly matches the observed ratios involving the $5.340 \mu\text{m}$ line.

3. RADIATIVE ATOMIC SHOCKS AND IR [Fe II] EMISSION

3.1. Shock Code and Model Parameters

The shock code that we use is the one developed by Raymond (1979) and improved by Cox & Raymond (1985), to which we have added the [Fe II] model described above. It solves the equations for a steady flow of the shocked gas as it cools, computing the time-dependent ionization state including photoionization. The line emissivities j_ν ($\text{ergs cm}^{-3} \text{ s}^{-1} \text{ sr}^{-1}$) of a fluid element are then calculated following its trajectory from the shock front until it cools down to 1,000 K or lower. These emissivities are integrated along the line of sight to obtain the line flux normal to the shock front, i.e.,

$$F_\nu = 2\pi \int j_\nu dx. \quad (7)$$

¹Bautista et al. (2015) provided the effective collision strengths and the branching ratios for radiative transitions in machine-readable forms in Tables 12 and 10, respectively. The numerical values in these tables, however, are not their recommended values but the 7-config model values in Table 8 and the TFDAC values in Table 4, respectively.

For shocks slower than about 110 km s^{-1} , the temperature jump is sensitive to the ionization fraction of preshock gas. If a substantial fraction of H atom is neutral, the effective temperature jump is reduced because a considerable fraction of shock energy is used in exciting and ionizing H atoms, which makes the H line intensities stronger. For the preshock ionization fraction of H, we adopt the result of Shull & McKee (1979). For He and heavier elements, we first calculate the shock structures assuming that they are in photoionization equilibrium with the interstellar radiation field, and then use the resulting shock radiation to calculate the ionization fraction of the preshock gas. The temperature structure at the shock front does not significantly affect the intensities of [Fe II] lines but does affect the ratios of the [Fe II] lines to the H lines.

We consider shock speeds $v_s = 20$ to 200 km s^{-1} and preshock densities of H nuclei from $n_0=10$ to 1000 cm^{-3} . The magnetic field strength B_0 limits the maximum density in the postshock layer and therefore the line intensity ratios. The [Fe II] lines are mainly emitted in the layer with moderate compression, and their ratios are not directly sensitive to magnetic field strength, though stronger fields imply lower densities and higher ionization states in the photoionized region where the [Fe II] lines form. According to Heiles & Troland (2005) and Crutcher et al. (2010), the magnetic field strength in the diffuse ISM ($n \leq 300 \text{ cm}^{-3}$) does not scale with density, and the median total magnetic field strength is $6 \mu\text{G}$. We adopt $5 \mu\text{G}$ as the tangential magnetic field strength in our models. We adopt the solar abundances by Asplund et al. (2009).

The models do not include emission from the photoionization precursor, which becomes important for shocks faster than about 150 km s^{-1} (Dopita & Sutherland 1996), although slower shocks in principle could produce an extensive precursor where $\text{Ly}\alpha$ ionizes Fe I to Fe II. However, the iron is strongly depleted ahead of the shock, and the precursor will contribute little to the [Fe II] emission. In the case of fast shocks in the LMC, where the precursor is not spatially resolved from the postshock flow, there may be significant hydrogen Pa β ($1.282 \mu\text{m}$) from the precursor.

3.2. Shock Structure and [Fe II] Emission

In radiative atomic shocks, an extended region of partially ionized gas develops behind the shocks, and this is where the [Fe II] emission originates. Below we describe the structure of radiative shocks and explore the emission characteristics of [Fe II] lines for two shocks of $v_s = 150$ and 30 km s^{-1} propagating into a medium of $n_0 = 10^2 \text{ cm}^{-3}$ and $n_0 = 10^3 \text{ cm}^{-3}$, respectively. The preshock gas is fully ionized in the former shock, while it is neutral in the latter shock.

Figure 5 (top frame) shows the temperature profile in the postshock cooling layer of the 150 km s^{-1} shock. The corresponding profiles of H nuclei and electron densities are shown in the bottom frame. At $N_{\text{H}} \sim 7 \times 10^{17} \text{ cm}^{-2}$ the cooling becomes important and

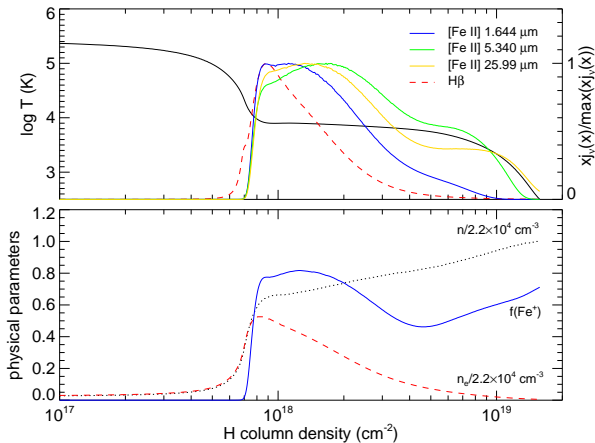


Figure 5. Structure of 150 km s^{-1} shock propagating into ambient medium of $n_0 = 10^2 \text{ cm}^{-3}$ and $B_0 = 5 \mu\text{G}$. The abscissa is H-nuclei column density swept up by shock. In the top frame, black solid line shows the temperature profile in logarithmic scale. Also shown are the normalized emissivities of [Fe II] and H β lines in linear scale. Note that we plot $xj_\nu(x)$ because the abscissa is in logarithmic scale. In the bottom frame, we plot the profiles of H nuclei density (n), electron density (n_e) and fraction of Fe in Fe $^+$ (Fe $^+$ /Fe).

temperature abruptly drops to 8,000 K. Then the temperature remains roughly constant over an extended region to $N_H \sim 1 \times 10^{19} \text{ cm}^{-2}$. This temperature plateau region is essentially an H II region where the heating is provided by UV radiation generated from the hot gas just behind the shock front. In contrast to HII regions around OB stars where H atoms are essentially fully ionized, however, the H ionization fraction is relatively low. Note that the gas density increases slowly in the plateau region while the electron density decreases logarithmically as the gas recombines. For the detailed description of the structure of radiative shocks, the readers may refer Shull & McKee (1979, and references therein).

In the bottom frame of Figure 5, we also plot the profile of Fe $^+$ fraction and, in the top frame, the emissivities of the [Fe II] 1.644, 5.340, 25.99 μm and H β lines. Note that the Fe $^+$ fraction is high and remains flat (0.4–0.8) far downstream, even reaching the region where $T \sim 1,000 \text{ K}$. The high Fe $^+$ fraction at $N_H \lesssim 5 \times 10^{18} \text{ cm}^{-2}$, i.e., in the region before the kink in the Fe $^+$ fraction profile, is due to collisions with electrons and to charge transfer with H atoms. But in the region beyond that, the gas ionization fraction is low and collisions with electrons become less important. Here, since the ionization potential of iron atoms is 7.9 eV, FUV photons from the hot shocked gas can penetrate far downstream to maintain the ionization state of Fe $^+$ where H atoms are primarily neutral. But as can be seen in the top frame, this extended Fe $^+$ region produced by FUV radiation does not contribute much to the [Fe II] forbidden line emission because of low electron density. Most of the NIR [Fe II] emission originates from the temperature plateau region where the ioniza-

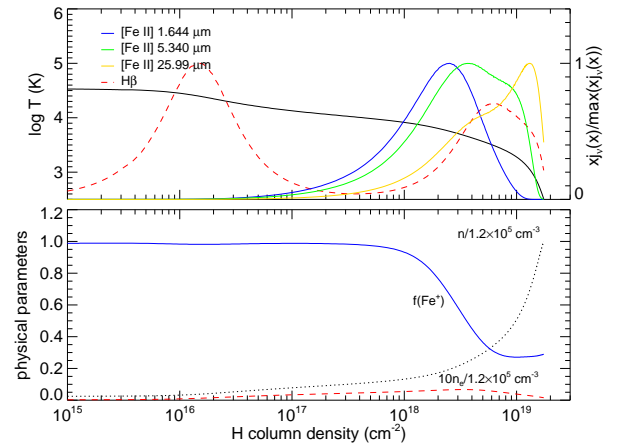


Figure 6. Same as Figure 5 but for 30 km s^{-1} shock propagating into ambient medium of $n_0 = 10^3 \text{ cm}^{-3}$ and $B_0 = 5 \mu\text{G}$.

tion fraction is not too low. The emissivity-weighted temperature and electron density of [Fe II] 1.644 μm (1.534 μm) line are 7,100 K (7,500 K) and $6,200 \text{ cm}^{-3}$ ($7,200 \text{ cm}^{-3}$), respectively. For comparison, the electron density that would have been derived from the ratio $F(1.534)/F(1.644) (= 0.13)$ is $5,400 \text{ cm}^{-3}$, somewhat lower than these. The [Fe II] 5.340 μm and 25.99 μm lines, whose critical densities are lower, are emitted from a more extended region than the NIR [Fe II] line emitting region. The emissivity-weighted mean temperature and electron density of these lines are $\sim 5,800 \text{ K}$ and $\sim 4,000 \text{ cm}^{-3}$. In Figure 5 we also show the emissivity of H β line. Note that the [Fe II] lines are emitted in a more extended region than the H β line, which is one of the reasons that the ratio of [Fe II] to H β lines from shocked gas is much higher than that in photoionized H II regions.

Figure 6 is the same plot for a 30 km s^{-1} shock. The temperature profile is not very different from that of the 150 km s^{-1} shock, except that we do not see an abrupt temperature drop and the resulting temperature plateau. This is because the incoming hydrogen is neutral, and a significant fraction of thermal energy is lost to its excitation. The strong H β emission at $\lesssim 10^{17} \text{ cm}^{-2}$ is from the collisionally excited neutral hydrogen. This emission is indeed stronger than that from the recombining H in the far downstream. Behind the shock front, Fe is mostly in Fe $^+$. (It was Fe $^{+2}$ for the 150 km s^{-1} shock.) [Fe II] lines are emitted where the fraction of Fe $^+$ is high and also the electron density is high. The [Fe II] 5.340 μm and 25.99 μm line emitting regions are shifted farther downstream compared to the 150 km s^{-1} shock case. (We have extended the calculation until the temperature drops to 300 K because significant 25.99 μm emission originates from the gas at $T_e \leq 1,000 \text{ K}$.) The emissivity-weighted temperatures for the 1.644, 5.340, and 25.99 μm lines are 7000, 5700, and 4400 K, respectively. The corresponding electron densities are 700, 680, and 630 cm^{-3} , re-

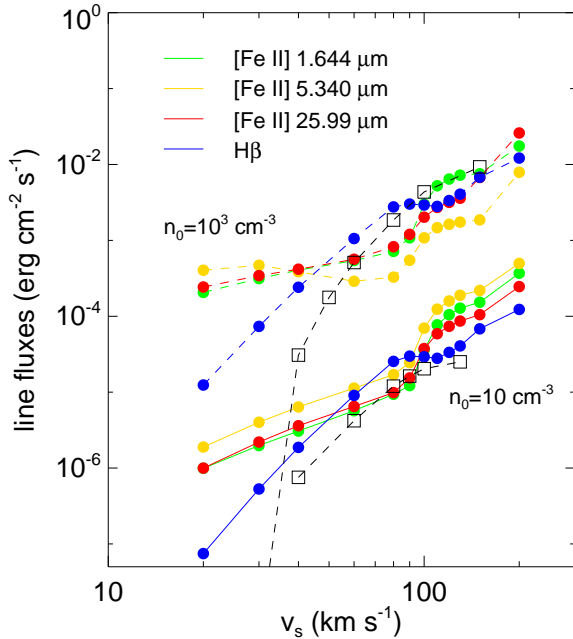


Figure 7. [Fe II] line fluxes normal to the shock front as a function of shock speeds for preshock densities 10 and 10^3 cm^{-3} . H β fluxes are also plotted for comparison. The filled circles along a constant preshock density line represent $v_s = 20, 30, 40, 60, 80, 90, 100, 110, 120, 130, 150,$ and 200 km s^{-1} . The empty squares are H β fluxes of Hollenbach & McKee (1989) and Shull & McKee (1979) for $n_0 = 10$ and 10^3 cm^{-3} , respectively.

spectively. The ratio $F(1.534)/F(1.644)$ is 0.045, which would yield $n_e = 700 \text{ cm}^{-3}$.

3.3. IR [Fe II] Line fluxes and Comparison with Other Shock Models

Figure 7 shows the fluxes of [Fe II] $1.644 \mu\text{m}$, $5.340 \mu\text{m}$, $25.99 \mu\text{m}$, and H β lines as a function of shock speed when $n_0 = 10$ and 10^3 cm^{-3} . If a constant fraction of the total shock kinetic energy flux $\rho_0 v_s^3/2$ is converted into a line radiation, the line flux will be proportional to v_s^3 . Indeed, H β fluxes at $v_s \geq 110 \text{ km s}^{-1}$ are well described by

$$F_{\text{H}\beta} \simeq 3.5 \times 10^{-4} \left(\frac{f_{\text{H}\beta}}{0.00575} \right) n_{0,2} v_{s,7}^3 \text{ erg cm}^{-2} \text{ s}^{-1} \text{ sr}^{-1}. \quad (8)$$

where $f_{\text{H}\beta} (\approx 0.6\%)$ is the fraction of incoming shock energy converted to H β line flux. The plateau in H β fluxes between about 70 and 110 km s^{-1} results from the collisional excitation contribution to H β when the preshock gas is partially neutral. At low shock speeds, a significant fraction of the shock energy is used to ionize the incoming neutral H, but the temperatures are low enough that more of the energy goes into Ly α and less into H β , so that the line flux drops faster (Raymond 1979) (see also Fig. 11 of Hollenbach & McKee 1989). The incoming hydrogen atoms are fully ionized at shock

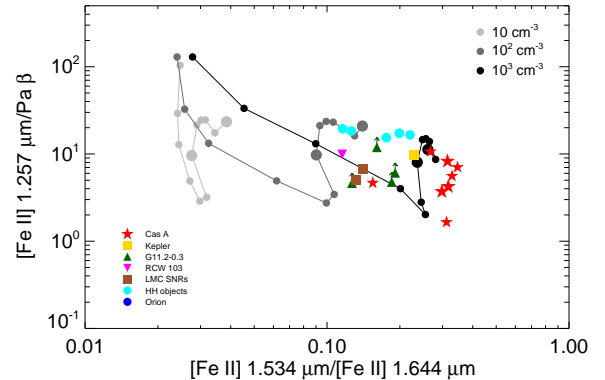


Figure 8. [Fe II] $1.257 \mu\text{m}/\text{Pa}\beta$ vs. [Fe II] $1.534 \mu\text{m}/[\text{Fe II}] 1.644 \mu\text{m}$ diagram. The lines of constant preshock densities are shown for $n_0 = 10, 10^2,$ and 10^3 cm^{-3} . Along each line, circles mark shock speeds of 20, 30, 40, 60, 80, 90, 100, 110, 120, 130, 150, and 200 km s^{-1} with 100 and 200 km s^{-1} marked by bigger circles. The abundance is solar.

speeds $\geq 110\text{--}120 \text{ km s}^{-1}$ independent of preshock density. In Figure 7, we compare our H β results to those of Hollenbach & McKee (1989) and Shull & McKee (1979) for $n_0 = 10^3$ and 10 cm^{-3} , respectively. The consistency among the different shock models is generally good. The line fluxes of Hollenbach & McKee (1989) are systematically lower than ours at low shock speeds because significant shock energy goes to H $_2$ dissociation and excitation, while we assume that the preshock gas is atomic.

Figure 7 shows that the [Fe II] lines are stronger than the H β line over most of the shock speed range when $n_0 = 10 \text{ cm}^{-3}$ and at low shock speeds when $n_0 = 10^3 \text{ cm}^{-3}$. The kink at $\sim 100 \text{ km s}^{-1}$ is probably because the UV radiation at the shock front becomes stronger, increasing the electron density in the [Fe II] emitting region.

We have also compared our results to those predicted by MAPPINGS III (Allen et al. 2008). For a shock with $v_s = 150 \text{ km s}^{-1}$, $n_0 = 100 \text{ cm}^{-3}$, and $B_0 = 5 \mu\text{G}$ for example, our code gives $F(1.644)/F(\text{H}\beta)$ of 2.1 and $F(1.257)/F(\text{Pa}\beta)$ of 16 which are a factor of 5 greater than those (0.40 and 3.1) of the MAPPINGS III. We note that the profiles of physical parameters for the same shock parameters are quite comparable except that the cooling starts later and the cooling region extends further in the MAPPINGS III code. Apparently the extent of the temperature plateau region where the [Fe II] lines originate is considerably ($\sim 1/2$) narrower in the MAPPINGS III case. We find that about half of the difference appears to originate from different choices of atomic rates. The other half may result from the treatment of the radiative transfer in the resonance lines.

Table 2
Observed NIR [Fe II] line ratios in SNRs and HH objects

| Name | Observed | | | A_V (mag) | Dereddened | | Ref |
|----------------------|-----------------------|-----------------------|-------------------------|----------------|-----------------------|-------------------------|-----|
| | $\frac{1.257}{1.644}$ | $\frac{1.534}{1.644}$ | $\frac{1.257}{Pa\beta}$ | | $\frac{1.534}{1.644}$ | $\frac{1.257}{Pa\beta}$ | |
| <u>Galactic SNRs</u> | | | | | | | |
| Kepler | 1.21 (0.00) | 0.22 (0.00) | ... | 1.3 | 0.23 | 9.70 | 1 |
| G11.2-0.3 C1 | 0.30 (0.02) | 0.14 (0.01) | > 5.32 | 16.5 | 0.19 | > 6.08 | 2 |
| G11.2-0.3 C2 | 0.26 (0.03) | 0.13 (0.03) | > 4.11 | 18.2 | 0.18 | > 4.76 | 2 |
| G11.2-0.3 C3 | 0.22 (0.02) | 0.09 (0.01) | > 3.95 | 19.7 | 0.13 | > 4.63 | 2 |
| G11.2-0.3 | 0.31 (0.01) | 0.12 (0.00) | > 10.47 | 16.1 | 0.16 | > 11.92 | 3 |
| Cas A | 0.85 (0.00) | 0.29 (0.00) | ... | 5.1 | 0.32 | 4.24 | 1 |
| Cas A | 1.67 (0.00) | 0.30 (0.00) | ... | 0.0 | 0.30 | 3.71 | 1 |
| Cas A | 0.73 (0.00) | 0.27 (0.00) | ... | 6.8 | 0.31 | 8.25 | 1 |
| Cas A | 0.80 (0.01) | 0.14 (0.02) | 4.45 (0.22) | 5.8 | 0.15 | 4.67 | 4 |
| Cas A | 0.64 (0.00) | 0.26 (0.02) | 1.55 (0.02) | 8.2 | 0.31 | 1.65 | 4 |
| Cas A | 0.64 (0.01) | 0.29 (0.08) | 6.59 (0.65) | 8.3 | 0.35 | 7.05 | 4 |
| Cas A | 0.63 (0.01) | 0.23 (0.02) | 9.95 (0.73) | 8.4 | 0.27 | 10.66 | 4 |
| Cas A | 0.63 (0.02) | 0.28 (0.02) | 5.22 (0.37) | 8.4 | 0.33 | 5.59 | 4 |
| RCW 103 | 0.88 (0.04) | 0.10 (0.01) | 9.50 (2.66) | 4.8 | 0.12 | 9.88 | 5 |
| <u>LMC SNRs</u> | | | | | | | |
| N49 | 1.33 (0.00) | 0.14 (0.03) | 6.65 (0.00) | 0.2 | 0.14 | 6.66 | 6 |
| N63A | 1.26 (0.00) | 0.13 (0.03) | 5.04 (0.00) | 0.8 | 0.13 | 5.07 | 6 |
| <u>HH objects</u> | | | | | | | |
| HH111F | 0.55 (0.01) | 0.14 (0.01) | 14.20 (4.26) | 9.9 | 0.18 | 15.38 | 7 |
| HH111H | 0.57 (0.01) | 0.10 (0.01) | 18.00 (6.01) | 9.5 | 0.12 | 19.43 | 7 |
| HH240A | 1.06 (0.01) | 0.21 (0.01) | 16.19 (1.01) | 2.8 | 0.22 | 16.55 | 7 |
| HH241A | 0.81 (0.03) | 0.11 (0.02) | 17.50 (5.85) | 5.6 | 0.13 | 18.32 | 7 |
| HH120 | 0.99 (0.02) | 0.19 (0.01) | 16.80 (4.20) | 3.5 | 0.20 | 17.28 | 7 |

Observed and dereddened line ratios. ‘...’ means not detected. The errors in parenthesis are usually 1σ statistical errors. ‘(0.00)’ means no errors are given. Observed line ratios are dereddened assuming the intrinsic ratio $[Fe II] 1.257 \mu m / [Fe II] 1.644 \mu m = 1.36$ and by using the Galactic extinction curve with $R_V = 3.1$. For the sources with the observed $[Fe II] 1.257 \mu m / [Fe II] 1.644 \mu m$ ratio > 1.36 , we adopted $A_V = 0$. The derived visual extinctions (A_V) are listed in the fifth column.

Comments on individual sources:

Kepler: $Pa\beta$ was not identified by Gerardy & Fesen (2001) but $Pa\gamma$ was. We have derived $[Fe II] 1.257 \mu m / Pa\beta$ assuming $Pa\beta / Pa\gamma = 1.83$ which is the ratio of Case B at $T_e = 7,000$ K.

G11.2-0.3: We have taken 3σ as an upper limit for $Pa\beta$.

Cas A: Same as the Kepler SNR.

N63A and N49: $[Fe II] 1.534 \mu m$ line had not been observed by Oliva, Moorwood, & Danziger (1990). But they observed $[Fe II] 1.600 \mu m$ line and obtained $[Fe II] 1.600 \mu m / [Fe II] 1.644 \mu m = 0.09 \pm 0.02$ and 0.08 ± 0.02 , which corresponds to $[Fe II] 1.534 \mu m / [Fe II] 1.644 \mu m = 0.14$ and 0.13 at $T_e = 7,000$ K.

References for the observed line ratios: (1) Gerardy & Fesen (2001); (2) Lee et al. (2013); (3) Koo et al. (2007); (4) Koo et al. (2013); (5) Oliva, Moorwood, & Danziger (1990); (6) Oliva, Moorwood, & Danziger (1989); Oliva et al. (2001); (7) Nisini et al. (2002)

4. SHOCK GRIDS AND COMPARISON TO OBSERVATIONS

4.1. NIR [Fe II] Lines

Figure 8 is a diagram of $F(1.257)/F(Pa\beta)$ vs. $F(1.534)/F(1.644)$ where the grids of constant preshock densities are plotted. The $F(1.257)/F(Pa\beta)$ ratio has a kink between 80 and 130 $km s^{-1}$ because the $Pa\beta$ flux remains flat in that velocity range (see Figure 7).

In Figure 8, we also plot the line ratios observed toward SNRs and Herbig-Haro (HH) objects (see Table 2). The SNR data points are believed to be associated with shocks propagating into the ambient medium, as we exclude observations of ejecta knots, although there could be some contamination from SN material. In order for comparison, we applied the extinc-

tion correction using the observed $F(1.257)/F(1.644)$ ratios. We also assumed some basic principles, e.g., the $F(Pa\beta)/F(Pa\gamma)$ ratio is given by that of Case B, if necessary (see the note in Table 2). The observed $F(1.257)/F(Pa\beta)$ ratios range from 2 to 20. For comparison, it is 0.02–0.03 in Orion bar (Walmsley et al. 2000).

Figure 8 shows that the observed line ratios toward SNRs and HH objects are well explained by shocks propagating at $v_s = 80$ – $200 km s^{-1}$ into a medium of $n_0 = 10^2$ – $10^3 cm^{-3}$ with solar abundances. (The two LMC points need to be shifted upwards in the diagram in order to be compared to the models because the Fe abundance in the LMC is about 1/2 of the solar abundance Russell & Dopita (1992).) According to Figure 8, the Cas A SNR shocks are experiencing the

Table 3
Observed MIR [Fe II] line ratios for SNRs and HH objects

| Name | $\frac{35.35}{25.99}$ | $\frac{24.52}{25.99}$ | $\frac{17.94}{25.99}$ | $\frac{5.340}{25.99}$ | $\frac{5.340}{17.94}$ | IRS mode | Ref |
|----------------------|-----------------------|-----------------------|-----------------------|-----------------------|-----------------------|------------|-----|
| <u>Galactic SNRs</u> | | | | | | | |
| Cygnus Loop | 0.27 (0.00) | 0.10 (0.00) | 0.27 (0.00) | NA | NA | SH, LH | 1 |
| Kes 69 | NA | 0.09 (0.01) | 0.25 (0.01) | 3.45 (0.22) | 13.88 (0.99) | SL, LL | 2 |
| 3C396 | NA | 0.14 (0.03) | 0.46 (0.01) | 3.08 (0.06) | 6.66 (0.12) | SL, LL | 2 |
| Kes 17 | NA | 0.06 (0.00) | 0.31 (0.02) | 3.66 (0.17) | 11.68 (0.81) | SL, LL | 2 |
| G346.6-0.2 | NA | ... | ... | ... | ... | SL, LL | 2 |
| G348.5-0.0 | NA | 0.09 (0.00) | 0.38 (0.00) | 5.02 (0.10) | 13.15 (0.26) | SL, LL | 2 |
| G349.7+0.2 | NA | 0.20 (0.00) | 0.51 (0.00) | 1.68 (0.02) | 3.28 (0.03) | SL, LL | 2 |
| W44 | 0.24 (0.00) | 0.03 (0.01) | 0.21 (0.00) | 4.78 (0.00) | 22.77 (0.00) | SL, SH, LH | 3 |
| W28 | 0.26 (0.00) | 0.06 (0.00) | 0.19 (0.00) | 3.38 (0.00) | 17.36 (0.00) | SL, SH, LH | 3 |
| 3C391 | 0.29 (0.00) | 0.08 (0.00) | 0.26 (0.00) | 2.42 (0.00) | 9.24 (0.00) | SL, SH, LH | 3 |
| IC443 | 0.91 (0.00) | <0.11 | 0.22 (0.00) | 2.80 (0.44) | 12.64 (2.00) | SL, SH, LH | 3 |
| <u>LMC SNRs</u> | | | | | | | |
| N63A SW | ... | 0.28 (0.00) | 0.49 (0.01) | 1.32 (0.16) | 2.67 (0.32) | All | 4 |
| N63A NE | 0.30 (0.00) | 0.20 (0.00) | 0.70 (0.00) | 1.13 (0.04) | 1.62 (0.06) | All | 4 |
| N63A SE | 0.29 (0.00) | 0.20 (0.00) | 0.53 (0.00) | 1.33 (0.10) | 2.52 (0.19) | All | 4 |
| <u>HH objects</u> | | | | | | | |
| HH54FS | 0.28 (0.05) | 0.07 (0.01) | 0.26 (0.05) | 2.58 (0.24) | 9.77 (2.20) | SL, SH, LH | 5 |
| HH54C | 0.27 (0.07) | 0.09 (0.01) | 0.33 (0.05) | 4.08 (0.47) | 12.55 (2.33) | SL, SH, LH | 5 |
| HH54EK | 0.41 (0.06) | 0.14 (0.02) | <0.36 | 1.88 (0.72) | > 5.20 | SL, SH, LH | 5 |
| HH7 | 0.34 (0.04) | <0.07 | <0.24 | ... | ... | SL, SH, LH | 5 |
| SMM1 blue | 0.30 (0.04) | 0.35 (0.02) | 0.26 (0.01) | NA | NA | SH, LH | 6 |
| SMM1 red | 0.28 (0.05) | ... | 0.15 (0.01) | NA | NA | SH, LH | 6 |

The numbers are surface brightness ratios. ‘NA’ means not observed, while ‘...’ means not detected. The errors in parenthesis are usually 1σ statistical errors. ‘(0.00)’ means no errors are given. The systematic errors in the Spitzer IRS fluxes have been estimated to be $\leq 25\%$ (Neufeld et al. 2006), so the uncertainties in the flux ratios would be $\leq 35\%$. Note that the lines obtained by different Spitzer IRS modules are from different areas, i.e., SH (9.9 - 19.6) and LH (18.7 - 37.2) modules in high resolution mode and SL (5.2-14.5) and LL (13.9-39.9) modules in low resolution mode.

Comments on individual sources:

Hewitt sources: Hewitt et al. (2009) did not separate the [Fe II] 25.99 μm line from the nearby [O IV] line, and they did not give any numbers for the [Fe II] 35.35 μm line. However, the 35.35 μm line is clearly seen on the wing of the [Si II] line in Kes79, 3C396, G48.5-0.0 and G349.7+0.2 at about 1/3 the strength of the 25.99 μm line. This plus the absence of any [Ne V] emission indicates that the 25.99 μm feature is dominated by [Fe II], though the presence of [Ne III] emission suggests that some [O IV] emission may be present.

References: (1) Sankrit et al. (2014); (2) Hewitt et al. (2009); (3) Neufeld et al. (2007); (4) Caulet & Williams (2012); (5) Neufeld et al. (2006); (6) Dionatos et al. (2014)

highest preshock densities of about $1,000 \text{ cm}^{-3}$, while the shocks in HH objects appear to have the fastest ($\gtrsim 150 \text{ km s}^{-1}$) shock speeds. The fact that the observations match models with solar abundances suggests nearly complete liberation of Fe from dust grains in these shocks.

4.2. MIR [Fe II] Lines

There are *Spitzer* MIR spectroscopic observations of various interstellar shocks. Table 3 lists the MIR [Fe II] line intensity ratios of some sources available in literature. They include SNRs and HH objects. The 25.99 μm line is the bright line between the lowest two levels and is available in all the spectra, so we have normalized the line intensities by the 25.99 μm line. The *Spitzer* IRS spectrometer, however, is composed of two, short and long wavelength, modules sampling different parts of the sky. Therefore, the ratios of the lines obtained from different modules could be far from what we would expect. In some cases, the emitting region

was mapped by rastering the slits (Caulet & Williams 2012; Dionatos et al. 2014), and in others it is possible to scale the fluxes in the different apertures by using lines in overlapping wavelength ranges of LL and SL modules (Hewitt et al. 2009) or by using lines in the different wavelength ranges that have known intensity ratios (Sankrit et al. 2014). We exclude ratios involving lines observed in different modules where neither method of normalization is possible.

Figure 9 is a diagram of $F(17.94)/F(25.99)$ vs. $F(24.52)/F(25.99)$. As we noted in § 3, the 17.94 μm line has nearly the same T_{ex} and n_{cr} as the 24.52 μm line, so the models lie along a straight line. (See the upper left frame in Figure 4. The plots in this section use the same line ratios as those in Figure 4.) The observed intensities are generally below the models, especially the protostellar jet SMM1 and the LMC SNR N63A SW. There is a considerable degeneracy in deriving shock speeds and/or preshock densities from these line ratios. For exam-

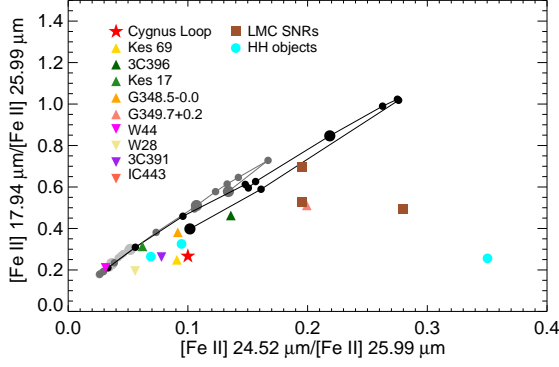


Figure 9. [Fe II] 17.94 $\mu\text{m}/[\text{Fe II}]$ 25.99 μm vs. [Fe II] 24.52 $\mu\text{m}/[\text{Fe II}]$ 25.99 μm diagram. The shock grids are the same as in Figure 8.

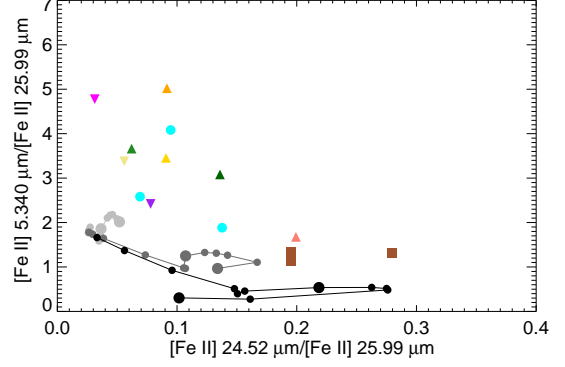


Figure 11. Same as Figure 9 but for [Fe II] 5.340 $\mu\text{m}/[\text{Fe II}]$ 25.99 μm vs. [Fe II] 24.52 $\mu\text{m}/[\text{Fe II}]$ 25.99 μm .

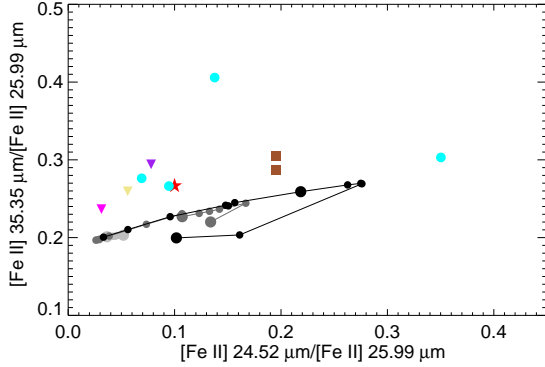


Figure 10. Same as Figure 9 but for [Fe II] 35.35 $\mu\text{m}/[\text{Fe II}]$ 25.99 μm vs. [Fe II] 24.52 $\mu\text{m}/[\text{Fe II}]$ 25.99 μm .

ple, the observed $F(17.94)/F(25.99)$ ratio ($= 0.27$) of the Cygnus Loop SNR would imply either $(n_0, v_s) \approx (10 \text{ cm}^{-3}, 120 \text{ km s}^{-1})$ or $(10^2 \text{ cm}^{-3}, 45 \text{ km s}^{-1})$ or $(10^3 \text{ cm}^{-3}, 25 \text{ km s}^{-1})$. According to a detailed shock modeling of the IR plus optical/UV spectra of the Cygnus Loop by Sankrit et al. (2014), a 150 km s^{-1} shock propagating into a medium of $n_0 \sim 5 \text{ cm}^{-3}$ can reasonably explain the observed spectra, so the first set of parameters is close to the right solution.

Figure 10 is a diagram of $F(35.35)/F(25.99)$ vs. $F(24.52)/F(25.99)$. Here the observed ratios lie above the predictions by $\lesssim 30\%$ over most of the $F(24.52)/F(25.99)$ ratio range, though one HH object lies much higher. Apparently, the result of the statistical equilibrium calculation appears to be in a better agreement with the observed $F(35.35)/F(25.99)$ ratios at high $F(24.52)/F(25.99)$ ratios (upper right frame in Figure 4). The poor agreement with the statistical equilibrium results at low $F(24.52)/F(25.99)$ ratios suggests that there are some fundamental issues in the $F(35.35)/F(25.99)$ ratios at low densities. The shock models using the coefficients of Bautista et al. (2015) yield an even larger offset as we can infer from Figure 4.

Figure 11 shows $F(5.340)/F(25.99)$ vs.

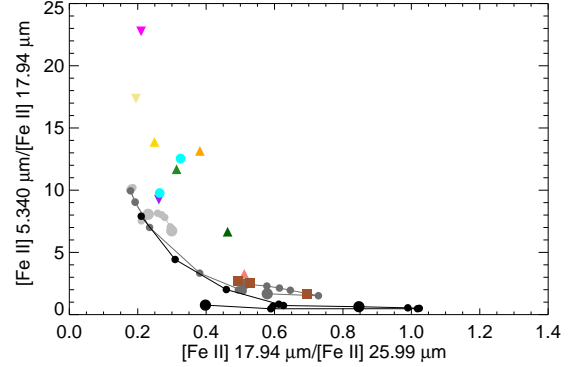


Figure 12. Same as Figure 9 but for [Fe II] 5.340 $\mu\text{m}/[\text{Fe II}]$ 17.94 μm vs. [Fe II] 17.94 $\mu\text{m}/[\text{Fe II}]$ 25.99 μm .

$F(24.52)/F(25.99)$. Here again, the observed $F(5.340)/F(25.99)$ ratios lie above the models, especially for low $F(24.52)/F(25.99)$ ratios. Figure 4 suggests that the presence of Fe^+ at higher temperatures would improve the agreement. But again the agreement is poor (by a factor of ~ 2) at low $F(24.52)/F(25.99)$ ratios, which seems to indicate that there are some fundamental issues in the $F(5.340)/F(25.99)$ ratios at low densities. Figure 12 presents $F(5.340)/F(17.94)$ vs. $F(17.94)/F(25.99)$, and it shows that although the 5.340 μm and 17.94 μm lines arise from neighboring levels the agreement is not better.

5. DISCUSSION

The results of the comparison of [Fe II] line intensity ratios predicted from the shock models to those observed in astronomical shocks may be summarized as follows. First, in the $F(1.257)/F(\text{Pa}\beta)$ vs. $F(1.534)/F(1.644)$ plane, the observed ratios fall on the model grids with reasonable range of shock parameters (Figure 8). So just based on this plot, the shock models appear to yield reasonably accurate relative fluxes of NIR [Fe II] lines. Second, among the MIR line intensity ratios, the $F(24.52)/F(25.99)$ and $F(17.94)/F(25.99)$ ratios predicted from the shock models both cover the

range of the observed ratios but do not yield consistent results for most data points (Figure 9). Third, $F(35.35)/F(25.99)$ ratios predicted from the shock models are smaller than the observed ratios by $\lesssim 30\%$ for most of the density range (Figure 10). Fourth, $F(5.340)/F(25.99)$ and $(F5.340)/F(17.94)$ ratios predicted from the shock models are significantly (by up to a factor of $\lesssim 5$) smaller than the observed ratios at all densities (Figures 11 and 12). In the following, we discuss the possible contributions of errors in the atomic physics, the shock wave models, and the observations to the problems.

5.1. Atomic physics

The first source of errors that we can think is an uncertainty in atomic parameters. Bautista et al. (2015) present several new calculations of the [Fe II] atomic rates and compare them with earlier calculations. They recommend the average of their computations, which is largely determined by four calculations using the Quinet, Le Dourneuf, & Zeippen (1996) target configurations for radiative transition rates. According to Bautista et al. (2015), the uncertainties in the radiative transition rates of the lowest 16 levels are generally better than 10 %. The $a^4F_{9/2}$ level where the 5.340 μm line originates has an exceptionally large uncertainty of 30%. The recommended values for collision strengths among the lowest states have an rms uncertainty of 10–50 %, and they are roughly half as large those given their DARC model or the R-MATRIX calculation of Ramsbottom et al. (2007). If the Einstein A coefficient of the 5.340 μm line were greater, the $F(5.340)/F(25.99)$ and $F(5.340)/F(17.94)$ ratios would have been in a better agreement with the observations. The largest offset between the predicted and the observed ratios in $F(5.340)/F(25.99)$ and $(F5.340)/F(17.94)$ are found at low density ends, which suggests an error in collision strengths rather than A coefficients.

One potential problem is that our model includes only 16 energy levels, and cascades from higher levels that are not included might influence the line intensities. We have used the CHIANTI package (Landi et al. 2013), which includes many higher energy levels, to estimate this contribution. (CHIANTI version 7 uses Fe II collision strengths from Zhang & Pradhan (1995), which are similar to those of Ramsbottom et al. (2007).) At 10^4 K, cascades contribute around 30% to the population of the upper levels of the lines we observe, but much of that comes from the levels that we include, and the contribution from higher levels would be smaller at the temperatures of 4,000 to 7,000 K where the bulk of the emission arises. We conclude that cascades from higher energy levels not included in the model probably do not affect the ratios considered here at more than the 20% level.

5.2. Shock models

The shock models are idealized in many ways. They assume a single shock speed and steady flow from the

shock until the gas reaches 1,000 K. What matters for the ratio-ratio plots is the distribution of Fe^+ ionization fraction over the density and temperature of the emitting region. Since the models span a reasonably broad range of parameters, they probably cover real parameters fairly well, even in cases such as the LMC SNRs, where the observed region undoubtedly includes a range of shock speeds. If the real shocks are incomplete, meaning that the gas does not have time to cool all the way to 1,000 K, the cool part of the Fe II emitting region would be absent, and that could affect the line ratios, but one would also expect places where the hotter part of the emitting region predicted in steady flow would be absent.

The models ignore emission from the shock photoionization precursor, but since the Fe is probably highly depleted ahead of the shock, that should be a good approximation. The radiation transfer in the model ignores resonant scattering, which is likely to be important for $\text{Ly}\alpha$ and the He I and He II resonance lines. Comparison with the MAPPINGS III model suggests that this may affect on the shock structure at a level as large as that caused by the atomic rate uncertainties, but it is not clear whether it would systematically change the ratio-ratio diagrams.

An interesting possible process not included in any model is that Fe atoms liberated from grains in the hot postshock gas will emit some [Fe II] photons before they are ionized to Fe III. The process has been observed in UV emission from C IV (Raymond et al. 2013), but the emission is very faint. The relatively low excitation rates of forbidden lines and the high ionization rate Fe II make it unlikely that this process contributes significantly to the observed fluxes.

5.3. Observational uncertainties

Extinction affects the NIR [Fe II] and Pa β lines, typically by 10% to 30% (e.g., see Table 2), and it is unlikely that errors in the extinction correction is a major contributor to the uncertainty. The *Spitzer* observations use different modules for the 5.340 μm and 17.94 μm lines than for the 25.99 μm and 35.35 μm lines, which could present a substantial uncertainty. We have included only observations where the region was mapped so that the flux from same area could be extracted, or where scaling of the channels using a known line ratio was possible. Moreover, the ratio-ratio plots show trends, such as good agreement at high densities and poor agreement at low densities, that are unlikely to arise from inconsistent treatment of the different channels. This argument would not apply to the outlying point at the top of Figure 10 or perhaps the HH object point at the lower right of Figure 9, however.

6. CONCLUSIONS

We find that the biggest obstacle to the interpretation of [Fe II] line intensities in the NIR and MIR ranges is still the uncertainty in the atomic rates for this complex ion. Neither of the most advanced calculations of

collision strengths gives a good match to the ratio-ratio diagrams of MIR lines, and the predicted ranges for some MIR line ratios are significantly offset from the observed ratios. While uncertainties in the shock modeling and the observations certainly exist, they seem less likely to resolve the problems.

The NIR line ratios can provide extinction to the source with an uncertainty of $A_V \approx 0.9$ mag and density of emitting region with an uncertainty of about 20%. The shock parameters derived from NIR line ratios might be reliable. The MIR line ratios, however, are sensitive both to density and temperature, although the density could be constrained to some range from ratios such as $F(17.94)/F(25.99)$ and $F(24.52)/F(25.99)$. The shock parameters may be obtained from MIR line ratios, but one should be cautious.

The most important application of the [Fe II] IR lines for interstellar shocks is probably the derivation of the iron abundance, often giving an indication of the fraction of refractory grains destroyed in the shock. Models predict that the mass liberated from silicate grains increases from near zero for a 50 km s^{-1} shock to around 40% for a 150 km s^{-1} radiative shock (Slavin et al. 2015). The ratio of the $1.257 \mu\text{m}$ line to $\text{Pa}\beta$ is consistent with this prediction if most of the shocks are faster than about 80 km s^{-1} . An indication of shock speeds would be the presence or absence of the [S III] line at 9532 \AA . Of the objects in Table 2, it is present in HH 240 and 241 and absent in HH 111 and 120. The gas phase abundance of iron can be estimated from the ratios of the NIR [Fe II] lines to [P II] $1.189 \mu\text{m}$ line or MIR [Fe II] lines to the [Ne II] $12.82 \mu\text{m}$ line (e.g., Giannini et al. 2008; Koo et al. 2013; Sankrit et al. 2014), since phosphorus and neon are not depleted onto grains. Sankrit et al. (2014) estimated an iron abundance around $1/2$ solar in a 150 km s^{-1} shock in the Cygnus Loop, but there was considerable spread in the ratios of observed to predicted intensities for the [Fe II] lines.

ACKNOWLEDGMENTS

This research was supported by Basic Science Research Program through the National Research Foundation of Korea(NRF) funded by the Ministry of Science, ICT and future Planning (2014R1A2A2A01002811). H.-J. Kim was supported by NRF(National Research Foundation of Korea) Grant funded by the Korean Government (NRF-2012-Fostering Core Leaders of the Future Basic Science Program).

REFERENCES

- Allen, M. G., Groves, B. A., Dopita, M. A., Sutherland, R. S., & Kewley, L. J. 2008, The MAPPINGS III Library of Fast Radiative Shock Models, *ApJS*, 178, 20
- Arnaud, M. & Raymond, J. 1992, Iron Ionization and Recombination Rates and Ionization Equilibrium, *ApJ*, 398, 394
- Asplund, M., Grevesse, N., Sauval, A. J., & Scott, P. 2009, The Chemical Composition of the Sun, *ARA&A*, 47, 481
- Bautista, M. A., Fivet, V., Ballance, C., et al. 2015, Atomic Data and Spectral Model for Fe II, *ApJ*, 808, 174
- Calet, A. & Williams, R.M. 2012, Infrared Spectral Mapping of Supernova Remnants. I. N63A and Its Environment, *ApJ*, 761, 107
- Cox, D. P., & Raymond, J. C. 1985, Preionization-Dependent Families of Radiative Shock Waves, *ApJ*, 298, 651
- Crutcher, R. M., Wandelt, B., Heiles, C., Falgarone, E., & Troland, T. H. 2010, Magnetic Fields in Interstellar Clouds from Zeeman Observations: Inference of Total Field Strengths by Bayesian Analysis, *ApJ*, 725, 466
- Deb, N. C., & Hibbert, A. 2010, Calculation of Intensity Ratios of Observed Infrared [Fe II] Lines, *ApJL*, 711, L104
- Deb, N. C., & Hibbert, A. 2011, Radiative Transition Rates for the Forbidden Lines in Fe II, *A&A*, 536, A74
- Dinerstein, H. 1995, Infrared Emission Lines as Probes of Gaseous Nebulae, The Analysis of Emission Lines: A Meeting in Honor of the 70th Birthdays of D. E. Osterbrock & M. J. Seaton, 134
- Dionatos, O., Jørgensen, J. K., Teixeira, P. S., Güdel, M., & Bergin, E. 2014, Atomic Jet from SMM1 (FIRS1) in Serpens Uncovers Protobinary Companion, *A&A*, 563, A28
- Dopita, M. A., & Sutherland, R. S. 1995, Spectral Signatures of Fast Shocks. II. Optical Diagnostic Diagrams, *ApJ*, 455, 468
- Dopita, M. A., & Sutherland, R. S. 1996, Spectral Signatures of Fast Shocks. I. Low-Density Model Grid, *ApJS*, 102, 161
- Draine, B. T. 2011, Physics of the Interstellar and Intergalactic Medium by Bruce T. Draine. Princeton University Press, 2011. ISBN: 978-0-691-12214-4,
- Gerardy, C. L., & Fesen, R. A. 2001, Near-Infrared Spectroscopy of the Cassiopeia A and Kepler Supernova Remnants, *AJ*, 121, 2781
- Giannini, T., Calzoletti, L., Nisini, B., et al. 2008, Near-Infrared, IFU Spectroscopy Unravels the Bow-shock HH99B, *A&A*, 481, 123
- Giannini, T., Antonucci, S., Nisini, B., et al. 2015, Empirical Determination of Einstein A-Coefficient Ratios of Bright [Fe II] Lines, *ApJ*, 798, 33
- Graham, J. R., Wright, G. S., & Longmore, A. J. 1990, Infrared Spectroscopy and Imaging of the Crab Nebula, *ApJ*, 352, 172
- Hartigan, P., Raymond, J., & Pierson, R. 2004, Infrared Emission Lines of [Fe II] as Diagnostics of Shocked Gas in Stellar Jets, *ApJL*, 614, L69
- Heiles, C., & Troland, T. H. 2005, The Millennium Arcicob 21 Centimeter Absorption-Line Survey. IV. Statistics of Magnetic Field, Column Density, and Turbulence, *ApJ*, 624, 773
- Hewitt, J. W., Rho, J., Andersen, M., & Reach, W. T. 2009, Spitzer Observations of Molecular Hydrogen in Interacting Supernova Remnants, *ApJ*, 694, 1266
- Hollenbach, D., Chernoff, D. F., & McKee, C. F. 1989, Infrared Diagnostics of Interstellar Shocks, in Proceedings of the 22nd ESLab Symposium, ed. B.H. Kaldeich (ESA SP-290; European Space Agency), 245
- Hollenbach, D., & McKee, C. F. 1989, Molecule Formation and Infrared Emission in Fast Interstellar Shocks. III - Results for J Shocks in Molecular Clouds, *ApJ*, 342, 306
- Koo, B.-C., & Lee, Y.-H. 2015, Near-Infrared Spectroscopy of Young Galactic Supernova Remnants, Publication of Korean Astronomical Society, 30, 145
- Koo, B.-C., Lee, Y.-H., Moon, D.-S., Yoon, S.-C., & Ray-

- mond, J. C. 2013, Phosphorus in the Young Supernova Remnant Cassiopeia A, *Science*, 342, 1346
- Koo, B.-C., Moon, D.-S., Lee, H.-G., Lee, J.-J., & Matthews, K. 2007, [Fe II] and H2 Filaments in the Supernova Remnant G11.2-0.3: Supernova Ejecta and Pre-supernova Circumstellar Wind, *ApJ*, 657, 308
- Landi, E., Young, P.R., Dere, K.P., Del Zanna, G. & Mason, H.E. 2013, CHIANTI Atomic Database for Emission Lines. XIII. Soft X-Ray Improvements and Other Changes, *ApJ*, 763, 86
- Lee, H.-G., Moon, D.-S., Koo, B.-C., et al. 2013, Wide Integral-Field Infrared Spectroscopy of the Bright [Fe II] Shell in the Young Supernova Remnant G11.2-0.3, *ApJ*, 770, 143
- McKee, C. F., Chernoff, D. F., & Hollenbach, D. J. 1984, Infrared Spectroscopy of Interstellar Shocks, in *Galactic and Extragalactic Infrared Spectroscopy*, eds. M. F. Kessler, J. P. Phillips (Reidel; Dordrecht), 103
- Montague, R. G., Diserens, M.J. & Harrison, M.F.A. 1984, A Measurement of the Cross Section for Electron Impact Ionisation of Fe+, *J. Phys. B*, 17, 2085
- Mouri, H., Kawara, K., & Taniguchi, Y. 2000, Excitation Mechanism of Near-Infrared [Fe II] Emission in Seyfert and Starburst Galaxies, *ApJ*, 528, 186
- Nahar, S. N. 1997, Electron-Ion Recombination of Fe II, *Phys. Rev. A*, 55, 1980
- Neufeld, D. A. & Dalgarno, A. 1987, Charge Transfer in Collisions of Doubly Charged Ions of Iron and Nickel with Hydrogen Atoms, *Phys. Rev. A*, 35, 3142
- Neufeld, D. A., Hollenbach, D. J., Kaufman, M. J., et al. 2007, Spitzer Spectral Line Mapping of Supernova Remnants. I. Basic Data and Principal Component Analysis, *ApJ*, 664, 890
- Neufeld, D. A., Melnick, G. J., Sonnentrucker, P., et al. 2006, Spitzer Observations of HH 54 and HH 7-11: Mapping the H2 Ortho-to-Para Ratio in Shocked Molecular Gas, *ApJ*, 649, 816
- Nisini, B. 2008, IR Spectroscopy of Jets: Diagnostics and HAR Observations, *Jets from Young Stars II*, 742, 79
- Nisini, B., Caratti o Garatti, A., Giannini, T., & Lorenzetti, D. 2002, 1-2.5 μ m Spectra of Jets from Young Stars: Strong Fe II Emission in HH111, HH240-241 and HH120, *A&A*, 393, 1035
- Nussbaumer, H., & Storey, P. J. 1988, Transition Probabilities for Forbidden Fe II Infrared Lines, *A&A*, 193, 327
- Oliva, E., Moorwood, A. F. M., & Danziger, I. J. 1989, Infrared Spectroscopy of Supernova Remnants, *A&A*, 214, 307
- Oliva, E., Moorwood, A. F. M., & Danziger, I. J. 1990, Infrared Spectroscopy of Supernova Remnants. II - A Detailed Study of RCW 103, *A&A*, 240, 453
- Oliva, E., Marconi, A., Maiolino, R., et al. 2001, NICS-TNG Infrared Spectroscopy of NGC 1068: The First Extragalactic Measurement of [P II] and a New Tool to Constrain the Origin of [Fe II] Line Emission in Galaxies, *A&A*, 369, L5
- Pradhan, A. K., & Nahar, S. N. 2011, Atomic Astrophysics and Spectroscopy, American Astronomical Society Meeting Abstracts
- Quinet, P., Le Dourneuf, M., & Zeppen, C. J. 1996, Atomic Data from the IRON Project. XIX. Radiative Transition Probabilities for Forbidden Lines in Fe II., *A&AS*, 120, 361
- Ramsbottom, C. A., Hudson, C. E., Norrington, P. H., & Scott, M. P. 2007, Electron-Impact Excitation of Fe II. Collision Strengths and Effective Collision Strengths for Low-Lying Fine-Structure Forbidden Transitions, *A&A*, 475, 765
- Raymond, J. C. 1979, Shock Waves in the Interstellar Medium, *ApJS*, 39, 1
- Raymond, J. C., Ghavamian, P., Williams, B. J., Blair, W. P., Borkowski, K. J., Gaetz, T. J. & Sankrit, R. 2013, Grain Destruction in a Supernova Remnant Shock Wave, *ApJ*, 778, 161
- Reilman, R. F. & Manson, S. T. 1979, Photoabsorption Cross Sections for Positive Atomic Ions with Z Equal to or Less than 30, *ApJS*, 40, 815
- Rodríguez-Ardila, A., Pastoriza, M. G., Viegas, S., Sigut, T. A. A., & Pradhan, A. K. 2004, Molecular Hydrogen and [Fe II] in Active Galactic Nuclei, *A&A*, 425, 457
- Russell, S. C., & Dopita, M. A. 1992, Abundances of the Heavy Elements in the Magellanic Clouds. III - Interpretation of results, *ApJ*, 384, 508
- Sankrit, R., Raymond, J. C., Bautista, M., et al. 2014, Spitzer IRS Observations of the XA Region in the Cygnus Loop Supernova Remnant, *ApJ*, 787, 3
- Shull, J. M., & McKee, C. F. 1979, Theoretical Models of Interstellar Shocks. I - Radiative Transfer and UV Precursors, *ApJ*, 227, 131
- Slavin, J. D., Dwek, E. & Jones, A. P. 2015, Destruction of Interstellar Dust in Evolving Supernova Remnant Shock Waves, *ApJ*, 803, 7
- Smith, N., & Hartigan, P. 2006, Infrared [Fe II] Emission from P Cygni's Nebula: Atomic Data, Mass, Kinematics, and the 1600 AD Outburst, *ApJ*, 638, 1045
- Verner, D. A., Ferland, G. J., Korista, K. T. & Yakovlev, D. G. 1996, Atomic Data for Astrophysics. II. New Analytic FITS for Photoionization Cross Sections of Atoms and Ions, *ApJ*, 465, 487
- Walmsley, C. M., Natta, A., Oliva, E., & Testi, L. 2000, The Structure of the Orion Bar, *A&A*, 364, 301
- Zhang, H. L., & Pradhan, A. K. 1995, Atomic Data from the Iron Project. VI. Collision Strengths and Rate Coefficients for Fe II., *A&A*, 293, 953